

The large Lower Centaurus-Crux moving group as seen by *Gaia* DR2

BERTRAND GOLDMAN^{1,2}

SIEGFRIED RÖSER^{3,4}

ELENA SCHILBACH^{3,4}

ATTILA C. MOOR⁵

THOMAS HENNING¹

¹*Max-Planck-Institut für Astronomie, Königstuhl 17, 69117 Heidelberg, Germany*

²*Observatoire astronomique de Strasbourg, Université de Strasbourg - CNRS UMR 7550, 11 rue de l'Université, 67000, Strasbourg, France*

³*Zentrum für Astronomie der Universität Heidelberg, Landessternwarte, Königstuhl 12, 69117 Heidelberg, Germany*

⁴*Zentrum für Astronomie der Universität Heidelberg, Astronomisches Rechen-Institut, Mönchhofstraße 12-14, 69120 Heidelberg, Germany*

⁵*Konkoly Observatory, Research Centre for Astronomy and Earth Sciences, Hungarian Academy of Sciences, H-1121 Budapest, Konkoly Thege Miklós út 15-17, Hungary*

(Received July 2, 2018; Revised April 30, 2022; Accepted April 30, 2022)

Submitted to ApJ

ABSTRACT

Scorpius-Centaurus is the nearest OB association and its hundreds of members have been divided into several large sub-groups, including Lower Centaurus-Crux. Here we investigate the stellar and substellar content of the Lower Centaurus Crux area using the *Gaia* DR2 astrometric and photometric measurements. We report the discovery of more than 1800 intermediate- and low-mass young stellar objects and brown dwarfs located in this area, that had escaped identification until *Gaia* DR2 provided accurate astrometry and photometry to perform a kinematic and photometric selection. The median distance of this region is 114.5 pc and 80% of the stars lie between 102 and 135 pc from the Sun. Our new members cover a mass range of 5 M_{\odot} to 0.02 M_{\odot} , with a completeness of 50% at the low-mass end, and add up to a total mass of about 700 M_{\odot} . The present-day mass function follows a log-normal law with $m_c = 0.22 M_{\odot}$ and $\sigma = 0.64$, and we find more than 200 brown dwarfs in our sample. The star formation rate had its maximum of $8 \times 10^{-5} M_{\odot} \text{yr}^{-1}$ at about 9 Myr ago. We grouped the new members in four denser subgroups, which have increasing age from 7 to 10 Myr, surrounded by “free-floating” young stars with mixed ages. The whole complex is presently expanding, and the expansion started between 8 to 10 Myr ago. Two hundred members show infrared excess compatible with circumstellar disks in various stages of evolution from full to debris disks. This discovery provides a large sample of nearby young stellar and sub-stellar objects for disk and exoplanet studies.

Keywords: open clusters and associations: individual (Lower Centaurus Crux) — stars: formation — brown dwarfs — protoplanetary disks — stars: luminosity function, mass function

1. INTRODUCTION

Co-eval structures of the Solar neighborhood are useful entities for various fields in astronomy. Either grav-

itationally bound (a.k.a. open clusters) or not (moving groups), they provide samples of stars that share the same composition, motion, and age. Possible deviations from this set of parameters also give insights into the formation of these structures: the velocity dispersion may allow to constrain the age and location of the birth place of the population; the composition and age dispersion may reveal a more complicated formation and multiple

stages of star formation. Co-evolution on the other hand lets us constrain the stellar evolutionary models. To find such structures in the Solar neighborhood allows spectroscopic follow-up of high spectral resolution and/or on small telescopes, and easy detection of low-mass members, making them particularly valuable.

For almost a century, the Scorpius-Centaurus OB-association (Sco-Cen) has been known as an ensemble of young, massive early-type stars, and which should hold the keys of star formation. Blaauw (1964) divided the huge nearby association into three subgroups, Upper Scorpius (US), Upper Centaurus Lupus (UCL) and Lower Centaurus Crux (LCC). Being on the southern hemisphere the quality of the astrometric data historically was always poorer than for associations on the northern hemisphere. Only with the advent of the Hipparcos data the situation changed, but only for a subset of the brightest stars. In their fundamental paper, using the Hipparcos measurements, de Zeeuw et al. (1999) presented an overview of the OB-associations in the wider neighborhood of the Sun. For Scorpio-Centaurus they obtained mean distances of 145 pc for US, 140 pc for UCL and 118 pc for LCC. Pecaut & Mamajek (2016) determined median ages of 11 (US), 16 (UCL), and 17 Myr (LCC), though each has a considerable spread of ages. Other authors obtained ages as low as 5 Myr for US (Preibisch & Zinnecker 1999; Preibisch & Mamajek 2008), and 16 (UCL) to 18 Myr (LCC) (Sartori et al. 2003; Mamajek et al. 2002).

In their introduction Wright & Mamajek (2018) give an excellent overview on the importance of the Sco-Cen complex for questions related to the modes of star formation. Using the observations from *Gaia* DR1 they confirmed that all three subgroups US, UCL and LCC are gravitationally unbound, and found neither evidence for expansion of the subgroups nor that they, or part of them, were formed by the disruption of star clusters.

In this paper, we use the results of *Gaia* DR2 (Gaia Collaboration et al. 2018) to uncover a large population of young stellar objects located at the east end of the ScoCen region, assembled in subgroups of increasing age. The paper is structured as follows: In Section 2 we describe the identification of the cluster and sub-clusters in the TGAS and *Gaia* DR2 catalogs; in Section 3 we determine and discuss the mass functions and age distributions of the groups. In Section 4 we discuss some interesting members, in particular those surrounded by circumstellar disks, and binaries. In Section 5 we study the internal dynamics and expansion of the groups. In Section 6 we summarize and discuss the major results of our paper.

2. DETECTION OF THE CRUX STAR FORMING REGION

2.1. Astrometric detection

Parallel to the cluster search program described in Röser et al. (2016), we ran an alternative search process better adapted to the finding of nearby co-moving groups. We give only a rough description of the procedure here as it is not crucial for this paper. The idea behind was to select a grid of convergent points homogeneously distributed over the sphere and to search for stars whose positions, proper motions and parallaxes are consistent with a given convergent point. We then selected stars which have at least 5 other stars within a radius of 10 pc around them and whose tangential velocities are consistent with the same convergent point. These we regarded as seeds of possible co-moving groups. Our search was restricted to stars having a parallax larger than 5.5 mas in TGAS. On the whole sky we found 706 of these seeds. Here we concentrate onto the area of the Scorpio-Centaurus OB-association (Sco-Cen) between Galactic longitude 280° and 360° and Galactic latitude from -20° to $+30^\circ$.

In Fig. 1 we present the result of our search in the area of Sco-Cen. In the background we show the stars from Hoogerwerf (2000) (US, UCL, LCC) by large gray squares. This serves as an indication of the extend of the Sco-Cen association. The seeds found by our search in TGAS are shown as black dots. Isolated seeds stand for small co-moving groups with not more than 6 stars in a 10-pc radius around the seed in TGAS. Spatial concentrations of seeds may suggest larger coherent groups. For instance, the concentration marked by the large cyan dot at $(l, b) = (344 \text{ deg}, +4 \text{ deg})$ is the young compact moving group around V1062Sco (Röser et al. 2018) at a distance of 175 pc. For comparison we also plot the centers of the two open clusters contained in MWSC up to 200 pc from the Sun (large red dots), as well as the groups found by Oh et al. (2017) with more than 5 neighbors (violet diamonds). In parts, their and our findings are overlapping. We retrieved the open cluster IC 2391 in MWSC at Galactic longitude $l = 289 \text{ deg}$. Even the poorly populated cluster Feigelson 1 (also known as the ϵ Chameleontis group, Feigelson et al. 2013) at $(l, b) = (300 \text{ deg}, -15 \text{ deg})$ was found as one seed. Of the other seeds, the concentrations at $(l, b) = (300 \text{ deg}, -1 \text{ deg})$ and the large group at $(l, b) = (297 \text{ deg}, +8 \text{ deg})$ seemed to be the most interesting, because of their proximity to the Sun; the mean of the TGAS parallaxes of these groups were 9.5 and 9.1 mas, respectively. We called the southern group Group A and the northern one Group B. The violet diamond in between Group A and B corresponds to the center of “Group 4” in Oh et al. (2017). Their group 4 actually comprises our groups A and B, and in their notation it has a size of 114 (number of stars in the group). It is worth mentioning that already Chereul et al. (1997)

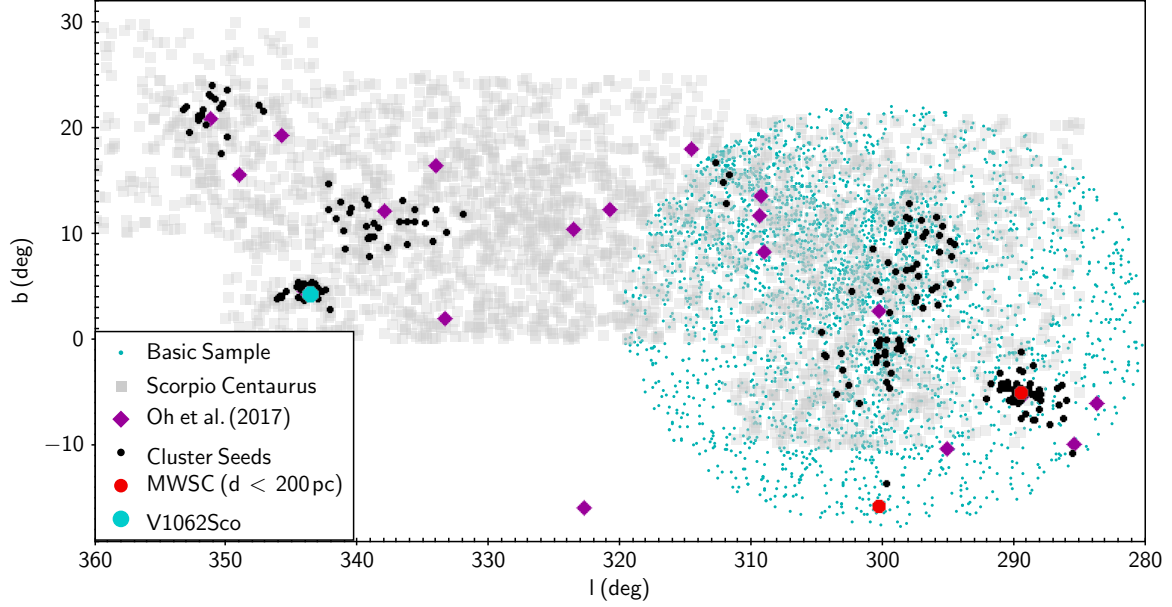


Figure 1. The Scorpio Centaurus Region. The axes are Galactic longitude and Galactic latitude in degrees. The grey squares in the background show the stars from Hoogerwerf (2000) and outline the ScoCen association. The black dots are the seeds of our cluster search in TGAS (see text). The small cyan dots outline the region studied in this paper and show the stars of our Basic Sample (BS, see text). The large cyan dot at $(l, b) = (344 \text{ deg}, +4 \text{ deg})$ is the young compact moving group around V1062Sco (Röser et al. 2018). The large violet diamonds are the groups found by Oh et al. (2017), and the large red dots mark open clusters in MWSC with distances less than 200 pc.

found a moving group of 33 nearby A-type dwarfs at a mean distance of 105 pc at $(l, b) = (304 \text{ deg}, +3 \text{ deg})$. For our Group A we determined the phase space coordinates on the basis of the TGAS positions, proper motions and parallaxes, as well as with radial velocities retrieved from SIMBAD, and found mean values of:

$$\begin{aligned} \vec{R}_c &= (x_c, y_c, z_c) = (-47.17, -5.23, -96.41) \text{ pc}, \\ \vec{V}_c &= (v_{x,c}, v_{y,c}, v_{z,c}) = (-2.97, 18.90, -14.76) \text{ km s}^{-1} \end{aligned} \quad (1)$$

in the Barycentric equatorial coordinate system with the X-axis pointing to the Vernal Equinox, the Y-axis to $\alpha = 90 \text{ deg}$ and the Z-axis points to the Equatorial North Pole. The vector \vec{R}_c is measured in parsec and is the position vector of the center of the group, and \vec{V}_c , in km s^{-1} , is the vector of the space velocity of the group; $\vec{V}_c / \|\vec{V}_c\|$ being the Cartesian equatorial coordinates of the convergent point.

Gaia DR2 now enables to study the groups A and B in great detail. In a first step we made a query of the *Gaia* DR2 catalog consisting of a cone search around $(\alpha, \delta) = (186.5^\circ, -60.5^\circ)$ with a radius of 20 degrees. Further we applied the following restrictions: for the trigonometric parallax $\varpi \geq 7 \text{ mas}$; for the proper motions $-43 \text{ mas/y} \leq \mu_{\alpha*} \leq -20 \text{ mas/y}$ ($\mu_{\alpha*} \equiv \mu_\alpha \cos \delta$), and $-35 \leq \mu_\delta \leq +12 \text{ mas/y}$. This query yielded 20,138 objects. The proper motion and parallax cuts were chosen to be consistent with the distribution of stars identified as members of these probable young moving groups we revealed in TGAS. For the further processing we followed the procedures described in Lindegren et al. (2018, Chapter 4.3 and Appendix C, Figs C.1 and C.2) to obtain a stellar sample cleaned from possible artifacts.

First, we required the “visibility periods used” to be equal to or larger than 7 (Eq. (11, ii) in Lindegren et al. 2018), which left us with 19,878 objects. The “unit weight error”-cut (Eq C.1 in Lindegren et al. 2018) removed a considerable portion of dubious entries, and 7,324 sources remained. Instead of the factor of 1.2 in this equation, we used a factor of 1.3 which seems more appropriate to our sample. As a next step we applied the “flux excess ratio”-cut (Eq C.2 in Lindegren et al. 2018) which reduced the sample to 3946 objects. Finally we discarded three stars with relative errors of parallaxes σ_ϖ / ϖ larger than 10 per cent. In summary, from the originally 20,138 entries in our search cone 3,943 sources survived these filterings, forming an astrometrically clean sample. For the subsequent discussion we always refer to this sample as “the Basic Sample (BS)”. The stars of the BS are shown in Fig. 1 as small cyan dots and outline the area of our search.

2.2. Candidate selection

In Fig. 2 we show the Color Magnitude Diagram (CMD) of the 3,943 stars of the BS, where we plot the absolute magnitude M_G (using the parallaxes from DR2) versus the color $G - G_{\text{RP}}$. For colors redder than about 0.4 mag two separate sequences show up, which we attribute to young stars (upper sequence) and old stars (lower sequence). We strengthen this in Fig. 3, where we also plot the theoretical isochrones of CIFIST (Baraffe et al. 2015) and Parsec (Marigo et al. 2017). The red line is the 40 Myr CIFIST isochrone, while the dotted red line is the 40 Myr Parsec isochrone. From a comparison between the two sets of isochrones for ages less than about 100 Myr, we found that the brighter part of the CMD

is appropriately described by the Parsec isochrones, whereas the CIFIST isochrones better fit the pre-main-sequence part for stars less massive than $1.4 M_{\odot}$. Here we note that the CIFIST isochrones use the pre-launch filter profiles of [Jordi et al. \(2010\)](#), while the Parsec isochrones use the profiles of [Evans et al. \(2018\)](#), both in the Vega system.

The lower black curve in Fig. 3 is the 400 Myr CIFIST isochrone representing old single stars, while the upper black curve would represent 400 Myr binaries of equal mass. This shows that the difference between the two observed sequences is so large that it cannot be explained by unresolved binaries of main sequence stars in this field. Consequently, the upper sequences must be attributed to young pre-main sequence stars. To separate the old and young population we made a cut along the 40 Myr CIFIST isochrone from the faintest stars up to the locus $(G - G_{RP}, M_G) = (0.34, 3.22)$, corresponding to $1.4 M_{\odot}$, and continue on the Parsec 40 Myr isochrone for brighter stars. The actual separation is shown in Fig. 4. We additionally discarded a small number of scattered stars which we attribute to older red giants. The subsample of young stars (2,659) in the BS is called “Young”, the complement (1,284 stars) “Old”. We note that beginning at the turnover at $(G - G_{RP}, M_G) = (0.75, 6.0)$ there may be increasing contamination by old binaries to the sample “Young”. Moreover, a small number of main sequence stars with $G - G_{RP} \leq 0.34$ may be also field stars, which can be identified and excluded by their different kinematics.

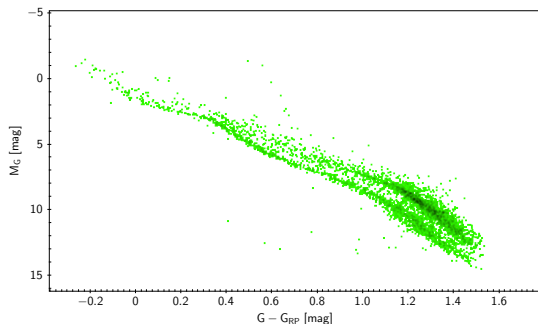


Figure 2. Absolute magnitudes M_G vs. $G - G_{RP}$ of the 3,943 stars of the basic sample (BS).

2.2.1. Extinction

Above we discussed the CMDs without considering possible extinction towards the sample of our stars from the BS. One may expect that its influence is rather small since our stars are all nearby ($\varpi \geq 7\text{mas}$). On the other hand, they are actually located within the Sco-Cen association and may not be far away from or behind gas and molecular clouds. In Figure 5 we show the color-absolute magnitude diagram M_{K_S} vs. $(J - K_S)$ for the stars from the BS which have counterparts in 2MASS ([Skrutskie et al. 2006](#)) together with the theoretical CIFIST and Parsec isochrones. In these passbands extinction would shift the stars mainly parallel to the abscissa with respect to the isochrones. From Figure 5 we first find that the 400 and 10 Myr isochrones perfectly demonstrate the mixture of old and young stars in the BS. Further, the 400

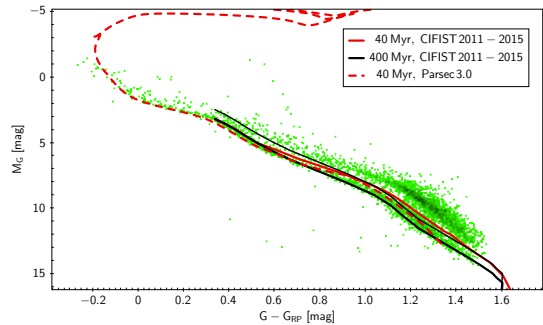


Figure 3. Absolute magnitudes M_G vs. $G - G_{RP}$ of the 3,943 stars of the basic sample (BS). The black curves are the 400 Myr CIFIST isochrones from [Baraffe et al. \(2015\)](#) for single stars (lower curve) and equal mass binaries (upper curve). The red solid line is the 40 Myr CIFIST isochrone, and the red dashed line the 40 Myr isochrone from Parsec3.0 ([Marigo et al. 2017](#)).

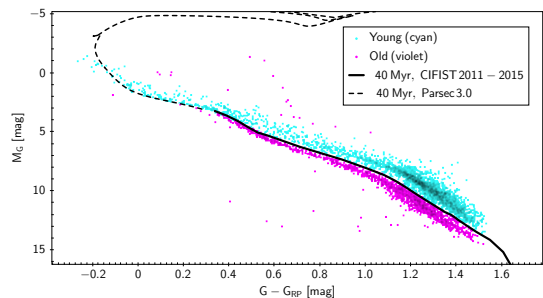


Figure 4. Absolute magnitudes M_G vs. $G - G_{RP}$ of the 3,943 stars of the basic sample (BS). The 40 Myr isochrone of ([Baraffe et al. 2015](#), solid line, masses less than $1.4 M_{\odot}$) and Parsec 3.0 (dashed line, masses higher than $1.4 M_{\odot}$) separate the young population (cyan) from the old population (violet).

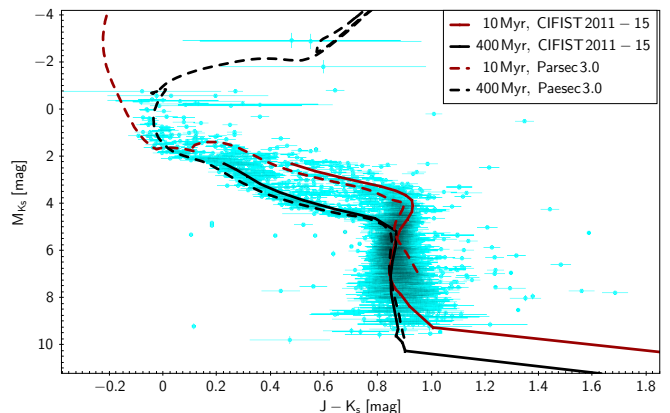


Figure 5. Absolute magnitudes M_{K_S} vs. $J - K_S$ of the stars of the BS. Shown are the 10 Myr and 400 Myr CIFIST isochrones of ([Baraffe et al. 2015](#), solid lines) and Parsec 3.0 (dashed lines).

Myr isochrones fit well the ZAMS of older stars of intermediate masses, and there is no reason to assume a significant

extinction towards the stars in the BS. The same findings hold for stars populating the vertical part of the isochrones at $(J - K_S) = 0.85$ mag. If these stars were de-reddened it would easily be seen as a blue-shifting in this CMD. However, any attempt to introduce a correction for de-reddening led to a poorer fitting of isochrones to observation in the CMDs Figs. 4 and 5. Of course we cannot exclude that individual stars may be significantly reddened. The extinction data published in *Gaia* DR2 does not allow to check this option as Andrae et al. (2018) mention in their paper. To summarize, we refrained from de-reddening the stars in the BS.

2.2.2. Kinematic analysis

To reveal the members of the potential moving group characterized by Eq. 1, we then studied the kinematics of the stars in the BS. Unfortunately, only about 12% of these stars have accurate radial velocities in *Gaia* DR2, with mean errors smaller than 2 km s^{-1} . Therefore, in order to identify co-moving stars, we have to rely on criteria based on their tangential velocities only.

For each star i from the BS we built the velocity vector $T\vec{V}_i = (tv_{x,i}, tv_{y,i}, tv_{z,i})$ which describes the components of its tangential velocity in the Cartesian Equatorial system (cf. Eq. 1) as:

$$\begin{bmatrix} tv_{x,i} \\ tv_{y,i} \\ tv_{z,i} \end{bmatrix} = \begin{bmatrix} \cos \alpha_i \cos \delta_i & -\sin \alpha_i & -\cos \alpha_i \sin \delta_i \\ \sin \alpha_i \cos \delta_i & \cos \alpha_i & -\sin \alpha_i \sin \delta_i \\ \sin \delta_i & 0 & \cos \delta_i \end{bmatrix} \cdot \begin{bmatrix} 0 \\ \kappa \mu_{\alpha*,i} / \varpi_i \\ \kappa \mu_{\delta,i} / \varpi_i \end{bmatrix}, \quad (2)$$

where $\kappa = 4.74047$ is the transformation factor from 1 mas yr^{-1} at 1 kpc to 1 km s^{-1} . Given a relatively large extension of our sample on the celestial sphere and the large range in distance, a co-moving sample of stars will, however, exhibit considerable variations in the components of $T\vec{V}_i$ simply because the proper motions $\mu_{\alpha*}, \mu_{\delta}$ are measured in a coordinate system which is not adapted to the space velocity of a group.

Therefore, we followed the algorithm of the convergent point method as described, e.g. in Röser et al. (2011), with the aim of representing the tangential velocities of each star with respect to axes parallel and perpendicular to the local vector to the convergent point. This is achieved in the following way: for each star i we define a coordinate system by 3 unit vectors $e_{1,i}, e_{2,i}, e_{3,i}$. The unit vector $e_{3,i}$ is given by the Cartesian equatorial coordinates of the i -th star as

$$e_{3,i} = \begin{bmatrix} \cos \alpha_i \cos \delta_i \\ \sin \alpha_i \cos \delta_i \\ \sin \delta_i \end{bmatrix} \quad (3)$$

The unit vector $e_{2,i}$ is defined as the cross product of $e_{3,i}$ and \vec{V}_c

$$e_{2,i} = \frac{e_{3,i} \times \vec{V}_c}{\|e_{3,i} \times \vec{V}_c\|}, \quad (4)$$

where \vec{V}_c is the space motion of the group from Eq. 1. Finally

$$e_{1,i} = e_{2,i} \times e_{3,i}. \quad (5)$$

The vectors $e_{1,i}$ and $e_{2,i}$ are unit vectors in the tangential plane pointing parallel and perpendicular to the direction of the convergent point. The observed components of the tangential velocity in this system are now given by: $v_{\parallel} = e_{1,i} \cdot T\vec{V}_i$ and $v_{\perp} = e_{2,i} \cdot T\vec{V}_i$. In an ideal case, where all the stars of a group would exactly move along the vector \vec{V}_c , v_{\perp} would become zero. This implies that we a priori know the vector \vec{V}_c with highest accuracy. But even in this case, internal velocity dispersion and uncertainties of the measurements will cause scatter in v_{\perp} .

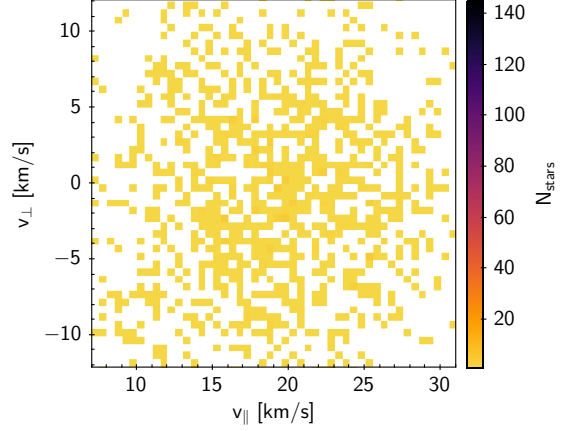


Figure 6. Distribution of the stars from the Old sample in the v_{\parallel}, v_{\perp} -plane with a binning of $0.5 \times 0.5 (\text{km s}^{-1})^2$. N_{stars} is the number of stars per bin.

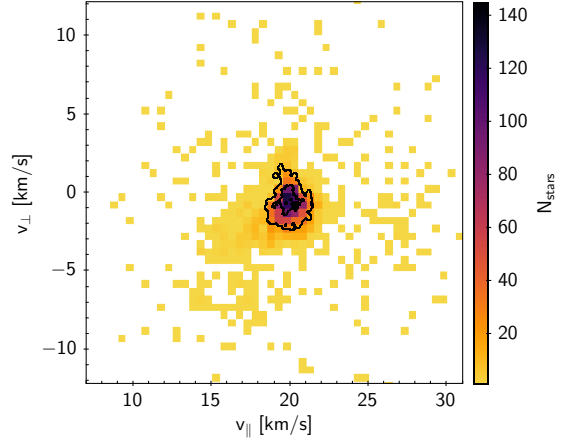


Figure 7. Distribution of the stars from the Young sample in the v_{\parallel}, v_{\perp} -plane with a binning of $0.5 \times 0.5 (\text{km s}^{-1})^2$. N_{stars} is the number of stars per bin.

We also determined the covariance matrix for the velocities v_{\parallel} and v_{\perp} according to error propagation from the covariance matrix of the $\mu_{\alpha*}, \mu_{\delta}, \varpi$. From the distribution of the variances we determined the mean and the 90% percentile of $\sigma_{v_{\parallel}}$ as 0.25 km s^{-1} and 0.36 km s^{-1} , respectively. The corresponding values for $\sigma_{v_{\perp}}$ are 0.08 km s^{-1} and 0.11 km s^{-1} .

Figures 6 and 7 show the distribution of the stars in the Old and the Young samples in the v_{\parallel}, v_{\perp} -plane with a binning of $0.5 \times 0.5 (\text{km s}^{-1})^2$. This bin size is large compared to the variances in v_{\parallel} and v_{\perp} , as we just showed. So, the distributions in Figures 6 and 7 present the true physical velocity dispersions of the BS. The different behavior of the old and young populations is obvious. The old stars (left image) are homogeneously distributed on the plane with a typical density of less than 3 stars per $0.5 \times 0.5 (\text{km s}^{-1})^2$. Such a flat distribution is fully consistent with the broad velocity dispersion of Galactic field stars. On the other hand, the velocity distribution of the young stars shows an impressive overdensity with a peak at $(20.25, -0.75) \text{ km s}^{-1}$ with a maximum of more than 150 stars per $0.5 \times 0.5 (\text{km s}^{-1})^2$. This overdensity is a strong signature for an autonomous coherent

group consisting essentially of stars younger than about 40 Myr (Fig. 4).

In Fig. 7 we define this group by manually cutting the stars falling into the peak mentioned above. Indeed they are populating the bins at a level of more than $30 N_{\text{Stars}}$. This cut is indicated by contour lines and the selected sample contains 1844 objects. We call this sample the Crux Group of Young Stars (CGYS) henceforth. In the following discussion we use barycentric Galactic

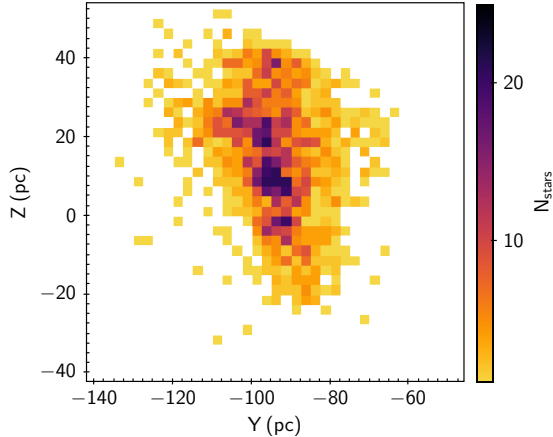


Figure 8. Density distribution of the stars from the CGYS projected on to the Y, Z plane (Galactic coordinates). The bin size corresponds to $2.5 \times 2.5 \text{ pc}^2$. N_{stars} is the number of stars per bin.

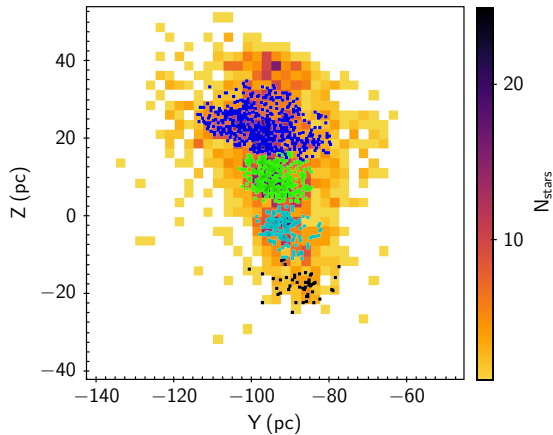


Figure 9. Same as Fig. 8, but overplotted by the stars of the sub-groups A0 (black), A (cyan), B (green) and C (blue).

Cartesian coordinates X, Y, Z instead of the equatorial coordinates as before. The axes X, Y, Z are directed to the Galactic center, the direction of Galactic rotation and to the Galactic north pole, respectively. The corresponding velocity coordinates are U, V, W . When we compare both samples, we find that, also in space, stars from the Old sample are distributed homogeneously, whereas the young stars, and especially the CGYS stars, exhibit stronger local concentrations. In Fig. 8 we present the distribution of the 1844 stars of the CGYS sample. Although these stars were selected in a narrow velocity range, they show a relatively broad distribution in space with several remarkable local overdensities.

This suggested to sub-divide CGYS into four subgroups (CGYS A0, CGYS A, CGYS B and CGYS C) shown in Fig. 9. The set of stars from CGYS not contained in Groups A0 to C is called CGYS Intergroup (CGYS Z). Let us mention here that this subdivision is somehow arbitrary, and was guided by the appearance of these groups already in Fig. 1.

The excellent quality ($\langle \varpi / \sigma_\varpi \rangle \geq 100$) of the individual parallaxes from *Gaia* DR2 in the region of CGYS allows to invert them into individual distances. The four sub-groups are not only distinguished by their position on the sky, but also by their different distances from the Sun. Figure 10 shows the distribution of the individual distances of the stars in the four sub-groups. There is a clear trend in distance from A0 as closest from the Sun to the largest sub-group C as farthest. Altogether, the whole CGYS, including the Intergroup members, extends from 102 to 135 pc from the sun (10 and 90% percentiles of the parallax distribution). The sub-groups A0 to C are more compact. The characteristic data

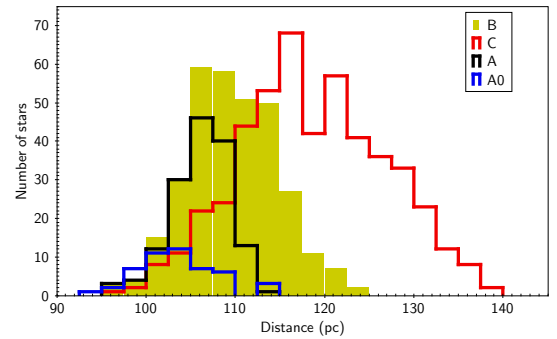


Figure 10. Distribution of the distances of the individual stars in the sub-groups of the CGYS derived from the trigonometric parallaxes from *Gaia* DR2.

for these groups are given in Table 1, while the data for individual members available in electronic format are described in Table 2. The spatial coordinates of the centers of the four subgroups are the means of the individual X, Y, Z of the N_{Stars} in each subgroup. The space velocities U, V, W of the groups are the averages of the individual velocities of those stars that have reliable radial velocity measurements in *Gaia* DR2. Therefore the values in Table 1 are derived from the observations in *Gaia* DR2 solely.

There are no sharp, physically justified boundaries in space between CGYS A0, A, B and C and the stars from CGYS Z. However, we will show in the following that, on average, they slightly differ not only by their location and kinematics, but also by their average age.

3. STELLAR MASSES AND AGES

3.1. Individual mass and age determination

The high photometric quality of *Gaia* DR2 enables a straightforward fit between the observed absolute magnitudes G , G_{BP} and G_{RP} and the ones determined from stellar evolution theory. We used two grids of models: the CIFIST 2011.2015¹ models for intermediate-mass stars down to the brown dwarf regime (Baraffe et al. 2015), and the PADOVA tracks Parsec 3.0² for the higher-mass stars (Marigo et al. 2017). We adopted $0.7 M_\odot$ as the limit between the two regimes, as the derived mass is identical for both

¹ phoenix.ens-lyon.fr/Grids/BT-Settl/CIFIST2011.2015/ISOCHRONES/

² stev.oapd.inaf.it/cmd

Table 1. Characteristic data of the sub groups of CGYS. The values are followed by the RMS.

Subgroup	N_{Stars}	X_G (pc)	Y_G (pc)	Z_G (pc)	U_G (km s ⁻¹)	V_G (km s ⁻¹)	W_G (km s ⁻¹)	D_{median} (pc)	age (yr)	Mass (M _⊙)
A0	49	52±3	-88±5	-17±3	-10.2±0.5	-19.4±1.0	-8.9±0.3	103.0	7.0	13
A	149	53±3	-92±3	-3±3	-9.5±0.7	-20.1±1.1	-7.9±0.3	106.5	7.2	50
B	317	55±8	-94±4	+10±3	-8.8±1.1	-20.2±1.8	-7.1±0.3	109.5	9.3	98
C	487	63±11	-97±8	+23±4	-8.2±1.1	-20.9±1.5	-6.1±0.6	118.0	10.0	249

Table 2. Content of the electronic table of the member parameters. Several *Gaia* DR2 columns, which are included for convenience without any change, are not described below.

Name	Description	Unit	Range
designation	<i>Gaia</i> DR2 designation
Group	group membership	...	A0,A,B,C,Z
ra, dec,...	<i>Gaia</i> DR2 parameters
vr_pred	predicted radial velocity	km s ⁻¹	5.56 ~ 16.6
vpar	observed tangential velocity toward the convergent point observed tangential velocity	km s ⁻¹	18.4 ~ 21.4
vperp	perpendicular to the convergent point direction	km s ⁻¹	-2.3 ~ +2.0
e_vpar	uncertainty on vpar	km s ⁻¹	0.053 ~ 1.28
e_vperp	uncertainty on vperp	km s ⁻¹	0.012 ~ 0.41
vparvperpcor	(dimensionless) correlation between	...	-0.83 ~ 0.79
X_gal	X galactic coordinate	pc	+26.1 ~ +102.7
Y_gal	Y galactic coordinate	pc	-134.0 ~ -64.6
Z_gal	Z galactic coordinate	pc	-30.6 ~ +51.0
age_CIFIST	age according to the CIFIST isochrones	Gyr	10 ⁻³ ~ 10 ⁻¹
mass_CIFIST	mass according to the CIFIST isochrones	M _⊙	0.026 ~ 1.4
Teff_CIFIST	effective temperature according to the CIFIST isochrones	K	2632 ~ 6766
logg_CIFIST	log ₁₀ gravity according to the CIFIST isochrones	CGS	3.4 ~ 4.9
age_P	age according to the Parsec isochrones	yr	5 10 ⁶ ~ 10 ⁸
mass_P	(initial) mass according to the Parsec isochrones	M _⊙	0.1 ~ 5.3
age	best age	Gyr	10 ⁻³ ~ 10 ⁻¹
mass	best mass	M _⊙	0.026 ~ 5.3
Teff_VOSA	effective temperature according to the VOSA fit	K	1200 ~ 7000
logL_VOSA	log ₁₀ bolometric luminosity according to the VOSA fit	Lbol _⊙	-3.6 ~ 2.4
age_VOSA	age according to the VOSA fit	Gyr	10 ⁻² ~ 0.21

models for that mass. We simultaneously determined the mass and age of each object by searching for the nearest model magnitudes to the data, after having linearly refined the model grid. We used the magnitudes in the filters G , G_{BP} and G_{RP} and only considered models up to 100 Myr.

We compared the model predictions in all three *Gaia* bands G , G_{BP} and G_{RP} and made a simply 3-d match between observed and theoretical data with a inverse relative weight of 1, 15. and 2.5 respectively, roughly corresponding to the *Gaia* photometric uncertainties.

3.2. Detection efficiency

In order to derive the mass functions of the groups, we first needed to determine our detection efficiency, in particular what fraction of members are lost due the selection cuts we applied to obtain a kinematically clean sample, as a function of the G magnitude and the sky location, which conjunctly for *Gaia* affects the most the precision and accuracy of the measurements.

For this, we considered all entries in the *Gaia* catalog over the sky region of interest, with parallaxes corresponding to the expected values of the groups' members, i.e. $\varpi > 7$ mas, and any proper motion, in order to have a good statistics. However distant objects entering the nearby sample and hopefully, and rightfully, removed by our selection cuts, should not lead us to underestimate the detection efficiency. To identify them, we used the *Gaia* color-magnitude diagram, looking for objects on the stellar main sequence to confirm the quality of their measured parallax and photometry. The main quality cuts which we applied (cf. section 2.1) are:

- “visibility periods used” cut: in the magnitude range of interest, the cut just removes 1–3% of the entries. Only 2% of the area has a detection efficiency lower than 70% and we do not correct for this effect.
- “unit weight error” cut: this cut removes 41% of the otherwise satisfactory entries, over a wide range of apparent magnitudes. Among those stars, 17% fall on the main sequence

(defined between the two 10 Myr and 1 Gyr isochrones; see red dots in Fig. 11) and may therefore be *bona fide* nearby stars with a roughly correct *Gaia* parallax (but possibly an erroneous uncertainty). As we removed those stars from further analysis, we may have lowered our sensitivity.

- “flux excess ratio” cut: 27% of the otherwise satisfactory stars fail this cut, mostly with $G > 19$ mag (see blue dots in Fig. 11), causing a severe loss of sensitivity at the faint end. Among those stars, 11% are located on the main sequence.

To correct our loss of sensitivity, we considered that the stars removed by either the “unit weight error” cut or the “flux excess ratio” cut but falling on the main sequence should be added to the nearby sample. For each G magnitude bin, we measured the fraction of stars passing all cuts and further analyzed, to the more completed sample derived above. In the mass functions, we increased the weight of each member candidate by that fraction.

In addition to those cuts, we selected stars with $\varpi > 10 \times \sigma_\varpi$. We can readily determine which fraction of our $\varpi > 7$ mas sample satisfies this cut, with more than 90% completeness down to $G = 19$ mag, and we corrected for it.

Finally, one needed to know the completeness of *Gaia* before any cut is applied. Ideally we would compare with a highly pure, deep optical catalog over the Crux sky region, but there are none. Comparing with the Pan-STARRS1 DR1 catalog (Chambers et al. 2016; Magnier et al. 2016), with a high-purity subset of objects with 20 or more detections, in two distinct fields with the same ecliptic latitude as the Crux field: $\epsilon = -45$ deg. We found very different 90% completeness limits, from $G = 20.7$ mag at a longitude of 129 deg, to a brighter limit of $G = 19.2$ mag at 90 deg. Instead we turned to the VVV near-infrared survey. Its second data release (Minniti et al. 2017) offers some overlap with the Crux region. We searched for *Gaia* counterparts to 5.10^5 VVV stars with null *pperrbits* in the Y and J bands, within $1''$. Transforming the near-infrared photometry to the G magnitude using the color transformation³:

$$G_{YJ} = Y_1 + 2.48(Y_1 - J_1) + 0.63, 0.4 < Y_1 - J_1 < 0.6 \text{ mag},$$

we determined that the *Gaia* 95% completeness limit is fainter than $G_{YJ} = 20$ mag.

Combining all those effects, we estimated our 50% completeness magnitude of $G = 19$ mag, which corresponds to a mass of $0.02 M_\odot$ for a 10-Myr CIFIST isochrone. We found no fainter candidates and did not attempt to constrain the mass function for lower masses.

The kinematic selection may also lead to the loss of some CGYS binaries, when their orbital motion is comparable or larger to the selection box size in the tangential velocity plane (see Fig. 7). For face-on, circular orbits, this will affect systems with a total mass $M_{\text{total}}/M_\odot > 10^{-2}a$ where a is the semi-major axis in A.U. Following Duchêne & Kraus (2013), this may affect a significant fraction of stars later than F, which have typical semi-major axis of tens of A.U. Early-type stars, with semi-major axis less than 1 A.U., may not be well fitted by the single-star astrometric model, and have been removed from the *Gaia* catalog.

3.3. Contamination

In the paragraph above we discussed the completeness of our sample using the observations of *Gaia* DR2. On the other hand, we also had to estimate a possible contamination to CGYS by “field” stars. Since we selected the 1844 stars of CGYS within a narrow range of tangential velocities (see Fig. 7), the contamination should be rather low. However, we cannot exclude the

³ Because the VVV fields cover the Galactic plane with $|b_{\text{gal}}| < 2$ deg, this relation depends strongly on extinction in the area and stellar sample considered. Here $l_{\text{gal}} = 295\text{--}318$ deg.

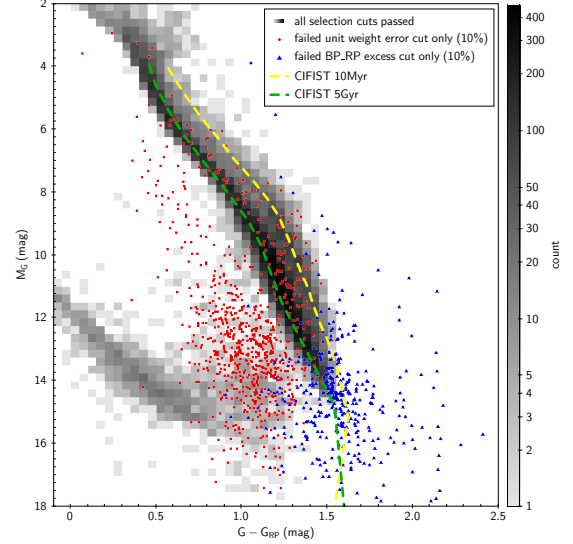


Figure 11. *Gaia* color-magnitude diagram of all sources in a 20-deg-radius area passing all the quality cuts (2-D histogram with gray scale); except the unit weight error or flux excess ratio cuts (red and blue dots resp., 10% statistics for readability)

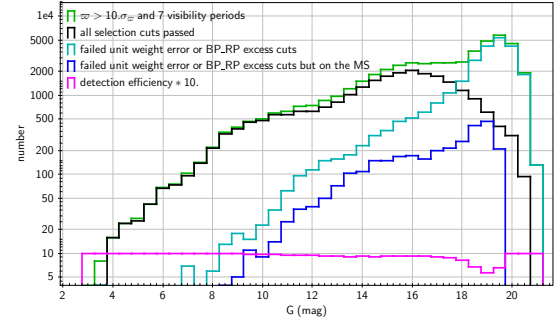


Figure 12. Total number of *Gaia* entries in a 20-deg-radius area with $\varpi > 7$ mas (red), and $\varpi > 10\sigma_\varpi$ and 7 visibility periods or more (green). The pale blue histogram shows all the sources passing all the quality cuts (2-D histogram with color scale) except the “unit weight error” (top-left panel) or “flux excess ratio” cut (top-right); while the blue histogram shows among those sources, those that are located on the main sequence (see Fig. 11).

possibility that there are, just by chance, a few young stars with the appropriate v_{\parallel} and v_{\perp} velocities but with an inadequate third component, the radial velocity. Provided that such stars have a roughly uniform distribution in Fig. 7, we derived the number of contaminants by comparing the average number density of stars in Fig. 7 in- and outside the area of CGYS. The 1844 stars of CGYS cover an area of $11 \text{ (km s}^{-1}\text{)}^2$. For the comparison we selected an area of $30 \text{ (km s}^{-1}\text{)}^2$ centered at $(26.5, 0) \text{ km s}^{-1}$, where we find 47 stars that we rated as a typical background in Fig. 7. This gives a possible contamination of 17 stars to our 1844 or about 1%. So, this has insignificant impact on the mass function of the CGYS.

3.4. Mass functions

As stated in Sec. 3.1 we determined masses of individual members by using the isochrones by Marigo et al. (2017) for masses higher than $0.7 M_{\odot}$. For lower masses we took the isochrones by Baraffe et al. (2015) as they model quite well the shape of the observed stellar and sub-stellar sequences for our objects in CGYS. Making corrections for incompleteness (Sec. 3.2), we determined the mass functions for all four groups, and for the inter-group members. They are shown in Fig. 13, top panel. We fitted a log-normal function (Scalo 1986) to our data, and present the mass functions of Salpeter (1955), Chabrier (2003), and Kroupa (2002) for comparison (see Fig. 13, bottom). We found that all the mass functions of our sub-groups are very similar and well reproduced by a single log-normal function of mean mass $m_c = 0.22 M_{\odot}$ with a dispersion of 8%, and a very consistent standard deviation $\sigma = 0.64$, hence slightly wider than the canonical Chabrier (2003) mass function (for systems) with $\sigma = 0.55$. In particular, we found no difference between the groups' mass functions and that of the inter-group members. Hence, the latter are not only low-mass members ejected by dynamical interactions. There is an excess at about $1.4 M_{\odot}$ which may have been caused by an imperfect separation between young and old stars.

The added-up masses of the members detected in each group are listed in Table 1. The total mass of the stars and brown dwarfs in CGYS is $673 M_{\odot}$.

We can compare our mass function to the mass functions reported for other young clusters or associations. Peña Ramírez et al. (2012) also used the isochrones from the Lyon group, NextGen98 (Baraffe et al. 1998), AMES-Dusty (Chabrier et al. 2000), and AMES-Cond (Baraffe et al. 2003), to determine the low-mass part of the mass function of the σ Orionis cluster with an age of 2 to 4 Myr. They slightly favor power laws over a log-normal form, with $\alpha = 0.6$ for masses less than $0.35 M_{\odot}$, where α is the index of the power law: $\Delta N / \Delta M = M^{-\alpha}$. Their log-normal fits in this mass range have σ between 0.57 and 0.64, so are comparable or slightly smaller than our value. They note however that this mass function considerably underestimates the number of planetary mass objects ($m < 0.012 M_{\odot}$), which is outside the mass range we are covering in this paper. While σ Orionis is a very compact cluster with a characteristic radius of only 1 pc (Béjar et al. 2011), CGYS is a more extended group of young objects. So, the star formation mode of both may differ.

Lodieu (2013) studied the Upper Scorpius part of the Scorpio Centaurus association, and found that for masses higher than $0.03 M_{\odot}$ is well reproduced by the log-normal form of the Chabrier mass function, independent of the age one determines for Upper Scorpius. This is a steeper decline from the $m_c = 0.22 M_{\odot}$ towards $0.03 M_{\odot}$ than we found for the neighboring Lower Centaurus Crux part. As Peña Ramírez et al. (2012) for σ Orionis, Lodieu (2013) finds an excess of objects with masses lower than $0.03 M_{\odot}$ depending on the adopted age. Again this is beyond the scope of this paper.

Very recently, Mužić et al. (2017) studied the deeply embedded young (≈ 1 Myr), massive and very dense star cluster RCW 38, and found $\alpha = 0.71 \pm 0.11$ for masses between 0.02 and $0.5 M_{\odot}$, a decline towards low masses even shallower than in σ Orionis.

Summarising, we found that the decline of our mass function from the mean mass of $0.22 M_{\odot}$ down to $0.03 M_{\odot}$ is steeper than that found for the σ Orionis cluster and RCW 38, but shallower than in the case of Upper Scorpius found by Lodieu (2013).

3.5. Age distributions

As mentioned above, we simultaneously determined the model masses and ages of individual members. For the mass and age determination for low-mass stars and sub-stellar objects we relied on the CIFIST isochrones. Firstly, because they model the observed loci of the object quite satisfactorily in all *Gaia* passbands, whereas in the case of the Parsec 3.0 isochrones, the magnitudes in the G_{RP} passband come out way too faint. This leads to the

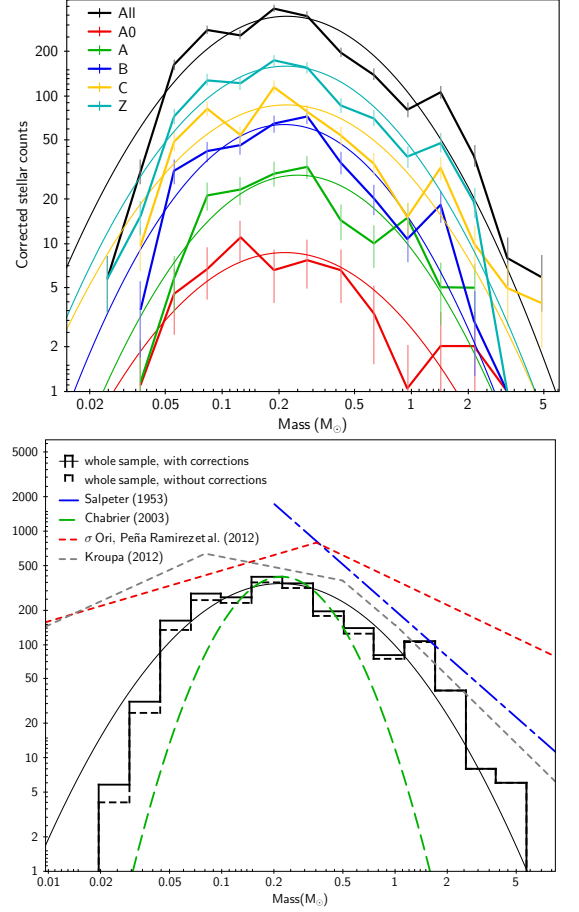


Figure 13. Top: Mass functions of all four groups (in color), the intergroup members (Z) and of the whole cluster (black), together with a log-normal fit. Bottom: Mass function of the whole cluster before (dashed histogram: stellar counts) and after (solid histogram) correction for incompleteness. We include various canonical mass functions, which we did not normalize for readability, as well as the power-law fit of the σ Ori cluster (Peña Ramírez et al. 2012).

situation that ages from Parsec 3.0 are lower than the CIFIST ones, when G_{RP} is included and higher, when it is not. The CIFIST isochrones for ages between 5 Myr and 40 Myr are mostly parallel to each other in the *Gaia* color-magnitude diagram. In Fig. 14 (top) we show the age distribution for each sub-group. The bulk of the ages is between 5 Myr and 20 Myr with few nominally older objects (note the logarithmic scale here). There are slight differences in the average ages of the subgroups of CGYS (shown in Table 1), increasing from as low as 7 Myr in A0 to 10 Myr for group C and the inter-groups members.

Fig. 14 (bottom) shows the star formation rate in the CGYS. We do not distinguish here between the sub-groups. Star formation essentially started 20 Myr ago and reached its maximum between 8 and 10 Myr before present with a rate of $8 \times 10^{-5} M_{\odot} \text{ yr}^{-1}$. For the young population in LCC Mamajek et al. (2002) found mean ages of the pre-main sequence stars from Hipparcos and TYC/ACT to range between 17 and 23 Myr. When using the Bertelli et al. (1994) tracks, they determined main-sequence turnoff ages for Hipparcos B-type members to be 16 ± 1 Myr. It is worth mentioning that much earlier de Geus et al. (1989) and de Zeeuw & Brand (1985) obtained turn-off ages between 10 and

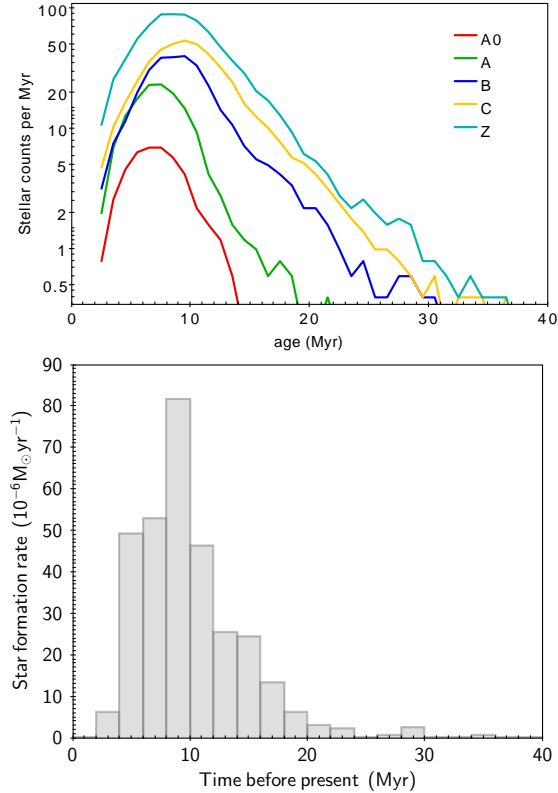


Figure 14. Top: CIFIST age distribution for each subgroup and the inter-group sample (Z). We stress that the stellar counts, measured for bins of width 5 Myr, are not independent. Bottom: The star formation rate in the CGYS as a whole as a function of time.

12 Myr, so much closer to the ages determined here. The difference between these earlier attempts to get an age for LCC and ours lies in the availability of *Gaia* DR2. Now, the majority of the members has masses way below those that could be used in the papers above, and the photometric quality is much superior. So, our age determinations rely on the evolutionary tracks of low-mass stars and brown dwarfs in the CIFIST isochrones and on Parsec 3.0 isochrones for masses higher than $0.7 M_{\odot}$.

4. REMARKABLE MEMBERS

4.1. Circumstellar disks

With ages below 20 Myr, a fraction of our CGYS members is likely to harbor a circumstellar disk at various stages of evolution.

We have used the Virtual observatory SED analyzer (VOSA Bayo et al. 2008) to analyze the spectral energy distribution of our members. In a nutshell, VOSA adjusts theoretical isochrones available in the Virtual observatory (VO) to the photometric information provided by the user and/or collected on the VO, by χ^2 minimization. It detects deviations from the photospheric emission, such as the infrared excess of interest here, and ignores the corresponding data points when the fit is repeated. We used all available VO photometry and fitted the data with the CIFIST models with Solar metallicity (Baraffe et al. 2015), refining once the infrared excess detection. The best model parameters are listed in Table 2. We then selected for further inspection those stars with an excess of at least 0.25 mag and 5σ , in at least one filter. We removed by eye a fraction of the candidates with clearly

poor fits. Finally we combined the official quality flags provided by the AllWISE catalog (Wright et al. 2010) and the results of a careful visual inspection of the relevant WISE images.

4.1.1. Identification of spurious WISE detections

Most of our excess candidates are located within 10° of the galactic plane. The higher source density as well as the bright extended background emission results in enhanced contamination and spurious detections in this region (Koenig & Leisawitz 2014). We took special care to identify and discard candidate sources affected by such issues. The AllWISE catalog already provides useful information on the data quality. We removed all targets where detection in any of the four bands was qualified to be spurious either because of a diffraction spike ("D" flag), scattered light halo ("H"), optical ghost image ("O") or latent image ("P") from a nearby bright source based on the "confusion and contamination flag" parameter of the AllWISE catalog. Sources found to be extended in the W3 or W4 bands (i.e. the reduced χ^2 of their profile-fit photometry, `w3rchi2` or `w4rchi2` is higher than 3) were also discarded. Furthermore, to ensure good quality data, only photometry with signal-to-noise ratio higher than 5 was kept in our analysis. According to Koenig & Leisawitz (2014), especially in regions with high sky background, a significant fraction of spurious detections may have remained unrecognized in the AllWISE catalog. To identify additional potentially problematic cases we inspected the WISE images of our excess candidates visually. This process revealed several additional fake sources, and also objects whose photometry is seriously contaminated by nearby bright sources or background nebosity. The applied quality criteria reduced the size of our sample to 171 systems. For 133 of them both the W3 and W4 bands data found to have good quality, for 38 objects the W4 band photometry was not used in the following analysis.

4.1.2. Classification of disk candidates

The observed infrared excesses, outlined by the WISE photometry, indicate the presence of circumstellar disks around our 171 selected stars. To assess the evolutionary stage of the revealed disks we applied the classification scheme proposed by Luhman & Mamajek (2012) and Pecaute & Mamajek (2016). This scheme allows to distinguish four different classes: full disks, transitional disks, evolved disks, and debris disks (for details of the different classes, see Espaillat et al. 2012) based on the $E(K_s - W3)$ and $E(K_s - W4)$ color excesses of the objects. To compute these color excesses the predicted photospheric $K_s - W3$ and $K_s - W4$ colors were taken from the VOSA models described above. Where no good quality W4 photometry was available the full, transitional, and evolved disk categories could not be distinguished unambiguously based on the applied criteria. For these cases we could discern three different categories based on the $E(K_s - W3)$ excesses: full or evolved disks, transitional or evolved disks, and debris disks. In three special cases the resulting classification was reconsidered based on literature data. Using the above scheme HD 110058, HD 121191, HD 121617 were classified as primordial disks. However, though these objects exhibit strong mid-infrared excess and harbor detectable amount of CO gas (Lieman-Sifry et al. 2016; Moór et al. 2017), they were generally categorized as debris disks based on their spectral energy distributions and dust masses (Melis et al. 2013; Lieman-Sifry et al. 2016; Moór et al. 2017). Considering these more detailed studies the three targets finally have been classified as debris disks. Color excesses as well as the obtained classifications are displayed in Fig. 15. As a result of our analysis we identified 119 primordial (full disks, transitional disks, or evolved disks) and 52 debris disks in our sample. The objects having disks are listed in Table 3 along with the main Simbad name and the discovery reference.

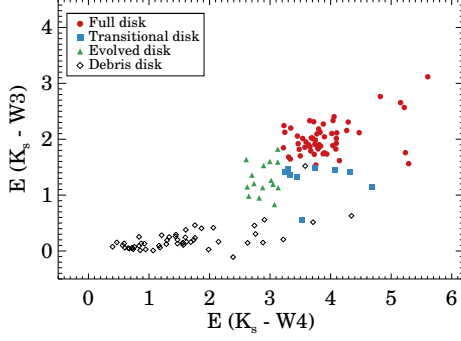


Figure 15. Color excesses for disk candidates having good quality photometry both in W3 and W4 bands. Classification of the disks is based on criteria proposed by [Luhman & Mamajek \(2012\)](#) and [Pecaut & Mamajek \(2016\)](#) (for details, see Sect. 4.1.2).

Table 3. Circumstellar disks found in CGYS. Col. 1 GAIA DR2 identifier, Col. 2 AllWISE identifier, Col. 3 Disk classification, Col. 4 Simbad compatible name, Col. 5 Reference for disk identification: 1 – [Carpenter et al. \(2005\)](#), 2 – [Chen et al. \(2005\)](#), 3 – [Chen et al. \(2011\)](#), 4 – [Chen et al. \(2012\)](#), 5 – [Clarke et al. \(2005\)](#), 6 – [Cotten & Song \(2016\)](#), 7 – [Cruz-Saenz de Miera et al. \(2014\)](#), 8 – [Fujiwara et al. \(2009\)](#), 9 – [Gregorio-Hetem et al. \(1992\)](#), 10 – [Mannings & Barlow \(1998\)](#), 11 – [Marton et al. \(2016\)](#), 12 – [Melis et al. \(2012\)](#), 13 – [Melis et al. \(2013\)](#), 14 – [Oudmaijer et al. \(1992\)](#), 15 – [Pecaut & Mamajek \(2016\)](#), 16 – [Rizzuto et al. \(2012\)](#), 17 – [Schneider et al. \(2012\)](#), 18 – this work

<i>Gaia</i> DR2 ID	AllWISE ID	Disk type	SIMBAD name	Reference
5240643988513310592	J111751.83-640205.6	Full	WRAY 15-788	15
5240643988513309952	J111758.09-640233.3	Debris	HD 98363	4
5346463427106534784	J112253.36-544610.5	Full/Evolved	...	18
5237215367676211072	J112912.74-653918.2	Full	WRAY 15-813	11
5345011040956367104	J113305.53-541928.6	Full/Evolved	HD 100453	9
5235954708871254144	J113842.48-670656.8	Evolved	...	11
5336376503118529536	J113930.08-590344.7	Evolved	...	11
5341805449189956992	J114541.34-575009.3	Transitional/Evolved	...	18
5344600820043829760	J114608.77-533150.1	Full	...	11
5368632811329281152	J114930.99-524328.7	Evolved	...	11
5335365467846055936	J114941.02-605541.9	Full/Evolved	...	18
5343960938637292800	J115014.25-553821.1	Full/Evolved	...	18
5233432944572581760	J115211.90-704155.9	Transitional	...	11
5371394166057656448	J115237.67-483908.8	Full	...	11
5343610331876174336	J115307.95-564338.3	Debris	HD 103234	2
5233349622203532160	J115317.63-710836.4	Full	...	11
5341470132513014272	J115626.51-584916.8	Debris	HD 103703	3
5368919371546982528	J115736.84-514612.1	Full	...	18
5859187277060333184	J120237.62-691132.2	Debris	HD 104600	4

Table 3 continued

Table 3 (*continued*)

<i>Gaia</i> DR2 ID	AllWISE ID	Disk type	SIMBAD name	Reference
6071149101451095552	J120301.88-591355.9	Full/Evolved	...	11
6072342483875171456	J120310.93-572322.5	Full	...	11
6126419661170559360	J120624.51-505415.3	Full	...	11
6125406255045171584	J120741.35-520921.8	Full	...	18
6126535483538801792	J120808.89-502655.9	Full	...	18
6126242639795170688	J120902.21-512041.0	Debris	TYC8241-2652-1	12
6129625905787938432	J120916.52-493929.0	Evolved	...	11
6071348491003883136	J120938.73-582058.8	Debris	HD 105613	4
6057558691062793856	J121022.12-620624.8	Full	2MASS J12102218-6206248	11
6071281833115416192	J121032.03-583753.8	Full	...	11
6072502291012793472	J121049.63-562643.3	Full	...	11
6072504073402829056	J121105.82-562404.9	Debris	HD 105857	4
6058704588327311744	J121109.08-601700.8	Full	...	11
6071307396762179200	J121131.37-581653.3	Debris	CD-57 4328	15
6054195353727048960	J121210.21-632714.8	Debris	HD 106036	4
5860803696599969280	J121213.07-655448.6	Full	...	11
6075840300923255424	J121356.05-550154.5	Transitional/Evolved	...	18
6054187038669456768	J121403.38-632821.6	Transitional/Evolved	...	18
5859345503663163776	J121454.56-681602.2	Full/Evolved	...	11
6130345536147985024	J121456.32-475654.6	Debris	HD 106473	4
6130049458282459264	J121555.04-484902.7	Full/Evolved	...	18
5854897321965963264	J121602.52-710303.5	Transitional	...	11
6126616095784535424	J121604.23-503934.2	Full/Evolved	...	18
6125486244513506944	J121610.32-521919.7	Full	...	18
5854827335488227840	J121625.70-712340.5	Evolved	...	11
5860789299912353024	J121706.25-654134.6	Debris	HD 106797	8
6072902994276659200	J121753.13-555831.9	Debris	HD 106906	2
6071727753787733120	J121857.96-573719.3	Debris	CD-56 4401	15
5860587917472173056	J122028.16-655033.7	Debris	HD 107301	4
6071432431847001088	J122054.89-582421.5	Full	...	11
6076319726660327424	J122102.33-535824.1	Full	...	11
6071734350857944704	J122201.42-573756.6	Debris	...	11
6125889730915656832	J122224.81-510134.5	Debris	HD 107649	3
6076435072302030976	J122233.20-533349.0	Debris	CD-52 5008	1
6053407828523827328	J122235.44-644158.7	Full	...	11
6071831039165476224	J122339.40-565228.7	Full/Evolved	...	11
6076173732132970368	J122728.71-540008.5	Full/Evolved	...	11
6127431486736144512	J122815.78-501812.6	Full	...	11
6071595258323070464	J123044.43-573132.3	Full/Evolved	...	18
6059507987719518976	J123046.21-581116.8	Debris	HD 108857	3
5842032249951369088	J123129.09-724949.5	Full	...	11

Table 3 continued

Table 3 (*continued*)

<i>Gaia</i> DR2 ID	AllWISE ID	Disk type	SIMBAD name	Reference
5859866294238119040	J123143.29-664814.5	Full	...	11
6128394830723278464	J123214.83-482625.6	Full	...	18
5856410391736766976	J123324.78-684855.5	Evolved	...	18
6127596855858449408	J123515.69-491228.9	Full	...	18
6074647919231574272	J123517.98-534944.0	Transitional	...	18
6077771803552535424	J123624.77-531144.4	Evolved	...	18
6079189967391903104	J123642.32-503613.2	Full/Evolved	...	18
6073522431640945152	J123658.71-551913.5	Full/Evolved	...	18
6061037064796017792	J123720.28-574152.6	Evolved	...	11
6073435948176417792	J123743.02-554851.1	Transitional/Evolved	...	18
5855753399177548416	J123842.70-684549.2	Debris	HD 109832	4
6079010918798704256	J123938.39-504240.4	Full	...	18
6127782196588876160	J123946.16-491155.6	Debris	HD 110058	10
6061230819360606080	J124013.37-564324.5	Full	...	11
6061152101197951104	J124330.40-570318.5	Full	...	11
5842130724965127040	J124337.41-715951.2	Full	...	11
6074699149583735552	J124356.50-533423.3	Evolved	...	11
6075075594872297216	J124401.90-533020.6	Debris	HD 110634	3
6061184846033257600	J124541.67-564312.0	Full	...	18
6074023259181420672	J124658.60-542648.2	Full	...	11
6061378871152834048	J124938.80-562730.0	Full	...	18
6073796965945655168	J125036.17-544007.2	Full	...	11
6135108448719442432	J125104.26-455341.8	Full	...	18
6074945440195177472	J125423.62-531111.2	Full	...	11
6057146614723101312	J125503.14-585041.0	Transitional	...	11
5843724192198636416	J125712.33-711934.6	Transitional	...	11
5857261551179958016	J125726.12-675738.6	Debris	HD 112383	4
6073874172274613248	J125810.01-541108.7	Debris	HD 112532	11
6135218228082010368	J125849.81-450025.0	Debris	...	18
6086025459381600512	J130102.36-465937.8	Full	...	18
6086135822861167872	J130459.41-472348.7	Debris	HD 113524	3
5862028930545927936	J130501.99-642629.8	Debris	HD 113457	4
5862081981988722048	J130505.23-641355.4	Debris	HD 113466	3
6081466678016078464	J130515.48-502438.9	Full/Evolved	...	11
5863636279063596800	J130614.82-611511.0	Transitional	...	11
6067520678700736768	J130758.91-550753.8	Evolved	...	11
6055854551117476480	J130916.14-601830.2	Debris	HD 114082	2
6066468652250246784	J130924.07-561643.4	Full/Evolved	...	18
6081858894428524928	J130948.62-495447.8	Evolved	...	11
6081961355170513536	J131039.42-491047.4	Full/Evolved	...	11
6134656652521100160	J131107.55-445553.1	Full/Evolved	...	18

Table 3 continued

Table 3 (*continued*)

<i>Gaia</i> DR2 ID	AllWISE ID	Disk type	SIMBAD name	Reference
6088022447375886080	J131327.52-454410.5	Debris	HD 114788	18
6080558825010747136	J131503.90-513107.3	Transitional/Evolved	...	18
6061902483556566144	J131505.64-594342.4	Evolved	...	11
6082109239483866752	J131650.56-481816.5	Full	...	18
6080641357101343616	J131723.21-512217.3	Full	...	11
6136589834475210752	J131728.90-425558.9	Debris	HD 115371	7
5869404140942539008	J131755.36-610039.0	Debris	HD 115361	3
6081726918673540224	J131815.63-495536.9	Full	...	18
6080650943468764160	J131855.48-510659.1	Transitional	...	11
6067245972584205568	J131909.90-543020.9	Transitional/Evolved	...	18
6083313960628561408	J131918.90-490359.7	Transitional	...	11
6061991269115435136	J131919.49-592820.6	Debris	HD 115600	2
6083262244920009088	J132026.77-491325.4	Debris	HD 115820	4
6083554337056984704	J132110.42-482748.7	Full/Evolved	...	18
6083320592058578816	J132124.03-485150.8	Full	...	18
5844296281847839232	J132207.47-693812.3	Full	PDS 66	14
6068501851076292864	J132231.92-521006.1	Debris	HD 116116	6
6083566882662827008	J132311.62-480432.9	Full	...	18
5844015768940264320	J132435.10-702026.2	Full	...	11
6063860919887691136	J132435.08-555724.2	Debris	HD 116402	3
6083482838752151808	J132544.65-474908.5	Debris	HD 116649	6
6083410236623985792	J132546.23-481956.8	Full	...	18
5870290798365685248	J133008.94-582904.3	Debris	HD 117214	2
6069015327310399104	J133052.30-521858.0	Full	...	11
5864076496104483072	J133129.96-644753.5	Full	...	11
6083039323239465472	J133155.53-481226.4	Full	...	18
6087637068551279360	J133239.21-442701.0	Debris	HD 117665	4
6063724889685860608	J133242.43-554939.4	Debris	HD 117620	6
6084228887439755648	J133312.87-461746.6	Full/Evolved	...	18
6062582943799800576	J133326.01-573057.2	Full	...	18
5863824329964744192	J133351.87-650833.3	Full	...	11
5863807042641766400	J133424.56-651747.5	Full	IRAS 13309-6502	15
6069078480506635520	J133700.16-520051.7	Full/Evolved	...	11
6070702390461240064	J133702.76-490940.3	Transitional/Evolved	...	18
6083123916915057152	J133738.24-473638.5	Transitional/Evolved	2MASS J13373825-4736397	18
6083123916915057664	J133738.37-473629.9	Evolved	2MASS J13373839-4736297	17
6084059360792776832	J133802.86-460801.6	Full	...	18
6111499666328784128	J133841.65-435602.6	Full	...	18
6108418181912503168	J133842.85-443058.8	Debris	HD 118588	4
6111450046567078400	J133921.34-435916.2	Full/Evolved	...	18
6108117706000646144	J134051.59-453531.6	Full	...	11

Table 3 continued

Table 3 (*continued*)

<i>Gaia</i> DR2 ID	AllWISE ID	Disk type	SIMBAD name	Reference
6106972427199739008	J134158.34-472302.6	Transitional	...	18
6108510472169485184	J134232.55-441356.4	Full/Evolved	...	18
6108176804749968640	J134457.31-451323.5	Debris	HD 119573	6
6107114951394253312	J134610.74-463410.6	Full/Evolved	...	18
5865593822062087168	J134635.35-620410.0	Debris	HD 119718	3
6066287438960606336	J134813.04-521010.7	Full	...	11
6065047911406764288	J134909.18-541342.3	Debris	HD 120178	3
6064679300141091328	J134918.90-553248.5	Evolved	...	18
6095022174615671168	J134922.23-470533.0	Full/Evolved	...	18
6093660880442332928	J134954.47-501424.0	Debris	HD 120326	3
6107537988493562752	J134959.21-454541.4	Transitional/Evolved	...	18
6066244867244361984	J135040.29-521734.5	Evolved	...	11
6093390744181536896	J135113.70-505243.4	Full	...	18
6065102435997739008	J135258.39-535846.1	Debris	HD 120795	6
6093891326905077632	J135308.17-484625.8	Full	...	18
6090407803495351296	J135509.96-504443.1	Debris	HD 121189	3
6065138792911302784	J135518.84-533142.8	Debris	HD 121191	13
6064911571962616576	J135619.94-540756.2	Debris	HD 121336	4
5871367460749900800	J135728.69-572803.1	Full	...	11
6095178206488363264	J135741.10-470034.4	Debris	HD 121617	10
6089254690680739200	J135910.66-524140.7	Full/Evolved	...	11
6091088744790298624	J140740.77-484214.7	Debris	HD 123247	10
6090811289904309504	J141121.25-492455.9	Full	...	11
6089894331566251904	J141419.61-503521.7	Full	...	11
5891843253451038976	J141837.96-584005.2	Transitional/Evolved	...	18
5892383216749227392	J141929.46-561501.1	Transitional/Evolved	...	18
5892631397138902528	J142859.40-555420.4	Full/Evolved	...	18
5897645926052184576	J143610.38-525633.8	Debris	...	11
5894194318558985984	J143750.19-545741.4	Debris	CD-54 5780	6

4.3. Resolved binaries

The *Gaia* DR2 catalog has a nominal spatial resolution of 0.4 arcsec, i.e. 46 A.U. at the mean member distance. According to [Duchêne & Kraus \(2013\)](#), about half the stellar binaries made of components with masses between 0.7 and 5 M_{\odot} have semi-major axis larger than that separation. These binaries, through their additional orbital motion, perturb the study of the internal dynamics of the cluster; and may lead to incompleteness (see Section 3.2). The mass functions that we analyzed in Section 3.4, are primarily system mass functions, but potential resolved binaries are counted individually. Finally, the orbits of high-mass systems with semi-major axis of a few tens of A.U. will ultimately be determined by *Gaia*, and therefore their dynamical masses of the components will be measured.

We searched our member catalog for pairs sharing the same proper motions and parallaxes. To estimate the contamination by random pairing, we used the standard procedure of creating a mock catalog of stars derived from the observed sample, shifting one coordinate by some angle, so that any pairing between the observed and mock catalogs can only be a spurious match. To

4.2. Brown Dwarfs

Given the small distance of the LCC and its young age, *Gaia* is able to detect even low-mass brown dwarfs in this region. Among the 1844 objects in the CGYS sample there are 214 with masses smaller than 0.073 M_{\odot} , i.e. brown dwarfs. Only for one of them, [FLG2003] eps Cha 16, we found an entry in SIMBAD. This young stellar object (YSO in SIMBAD) has spectral type M5.75 (we determined $M_G = 11.51$, mass = 0.05 M_{\odot} , age = 7 Myr), is located at the farthest edge of the CGYS sample, and is a member of our A0 Subgroup. War Among those 214 brown dwarfs, 34 harbor a circumstellar disk. While we are not complete with respect to transitional and debris disks that are too faint to be detected with our WISE selection, we note that $(14 \pm 3)\%$ of the brown dwarfs bear full disks or full/evolved disks. This is eight times higher (a 5σ effect) than for stars with a fraction of $(1.6 \pm 0.5)\%$, possibly meaning that brown dwarfs keep their disk optically thick at infrared wavelengths longer than stars.

estimate the quality of the match, we calculated the sum Σ of the differences between the proper motions and parallaxes, expressed in σ . We include in the error budget the orbital motion, which will introduce a difference in the proper motions, calculated for a face-on, circular orbit.

We selected observed pairs up to 10 arcmin and $\Sigma < 9$. For each pair, we determined the number of spurious pairs with parameters (sky separation, Σ) smaller than the observed pair, i.e. better matches. To improve the statistics, we shifted the observed sample either RA or DEC by 0.5, 1, and 1.5°. We identified 8 pairs, with separation up to 3', for which the number of better spurious matches is smaller than 2.2. They are listed in Table 4. The next best candidate, with a separation of 400'' and $\Sigma = 7.2$, have 20 better spurious matches.

Although the statistics is limited, we find that the mass ratios increase from 0.1–0.2 for F, G stars to almost unity at the end of the main sequence, as has been found in previous studies (for a review, see Duchêne & Kraus 2013). The lowest-mass pair we identified has a total mass of 0.4 M_{\odot} , and the closest separation is 3 arcsec.

5. THE MOTION OF CGYS

Inspecting Table 1 we discovered correlations between the spatial coordinates and the respective velocities of the sub-groups. This suggests an expansion of the whole CGYS. We therefore used these space motions to trace the groups back in time to find the minimum extension of the whole complex. Given the ages of the stars in CGYS, we trace them back for not more than about 20 Myr. So, we used a simple linear approach $x(t) = x(0) + t \times u$ with x in parsec and u in pc Myr^{-1} ($1 \text{ km s}^{-1} = 1.0227 \text{ pc Myr}^{-1}$). To characterize the size of the CGYS, we used the quantity

$$R_{rms} = \sqrt{\sum_{i=0}^N \sum_{j=i+1}^N r_{i,j}^2} \text{ where } r_{i,j} \text{ is the 3-d distance between}$$

sub-group i and subgroup j . We traced back the centers of the subgroups in steps of 0.1 Myr, and found that R_{rms} had a minimum at -10 Myr, i.e. 10 Myr ago. This finding is compatible with the ages estimated for the individual stars in CGYS.

In this connection the question arose if the sub-groups we see now, were also separated from the beginning. To test this hypothesis it is necessary to trace back the individual stars of the CGYS sample, which means we need accurate radial velocity measurements for a representative subset of stars in CGYS. In *Gaia* DR2 we find observed radial velocities for 247 stars of the CGYS. The formal precision of the radial velocity measurements varies between 0.2 and more than 10 km s^{-1} with a median of 2 km s^{-1} . These values are at least one order of magnitude poorer than for the tangential velocities. This creates a problem for a direct backtracing of the stars. It influences primarily the Y coordinate, because it is closest to the line-of-sight. To a lesser extend this holds for the X and Z coordinates.

To reduce the influence of the poorly measured radial velocities, we excluded the Y coordinates from the calculations and considered only stars having $\sigma_{V_{r,obs}}$ better than 2 km s^{-1} for the backtracing. The minimum radius R_{rms} of 15.2 pc (from X, Z only) is reached at -9 Myr, while at present it is 25.3 pc. The result is shown in Fig. 16. From left to right we show the distributions of the 123 stars at present, 9 Myr ago and 18 Myr ago. The positions of the stars 18 Myr ago are shifted by 50 pc in the positive Z -direction to avoid overlap. Already at -9 Myr and even more at -18 Myr we notice 11 outliers which we had excluded from the calculation of the radius R_{rms} .

We conclude that the CGYS as a whole is expanding since at least 9 to 10 Myr, and the sub-groups A0 to C, which we observe today, were parts of a single structure at that time. The clumps are probably the results of slightly different initial space velocities. We cannot exclude that expansion already started more than 10 Myr ago as backtracing is hampered by the poor knowledge of

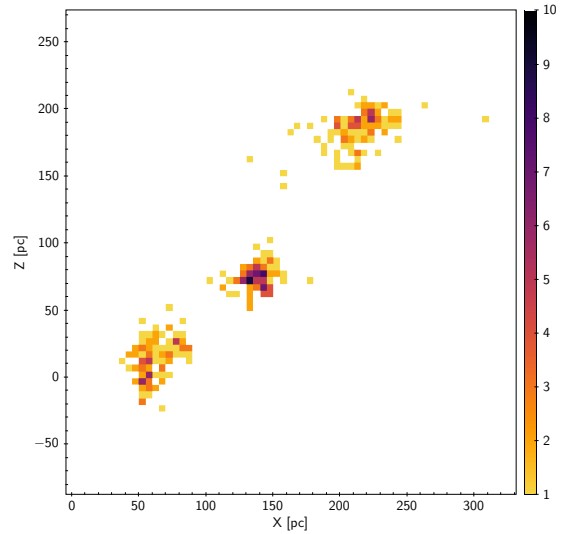


Figure 16. Density distribution of 123 CGYS stars having accurately measured radial velocities (see text). The most left distribution shows the configuration at present, the central one 9 Myr ago and the right one 18 Myr ago. The latter is shifted by 50 pc in the positive Z -direction to avoid overlap with the configuration at -9 Myr.

radial velocities (2 km s^{-1} at 10 Myr make an offset of 20 pc). Although 70% of the stars in CGYS were estimated to be younger than 10 Myr, the onset of star formation could have started earlier, and a later event triggered expansion. Wright & Mamajek (2018) find no indication of expansion in their careful analysis of the kinematic history of LCC on the basis of *Gaia* DR1. In hindsight this may be caused by the 6 to 9 times lower accuracy of the TGAS proper motions compared to those in DR2, a figure which we get from a comparison of the 161 TGAS stars in common with the 1844 stars from the CGYS sample.

In this context, we mention that de Geus (1992) also found no expansion in the region of Crux, but from a completely different approach. He examined the distribution of neutral Hydrogen gas (H1) connected to the Sco-Cen association. Whereas the column density of H1 is low over most of the area of CGRS, he found an H1 loop (shell) at $(l, b) = (285 \text{ deg}, +18 \text{ deg})$, and determined its center to be at $(l, b) = (300 \text{ deg}, +8 \text{ deg})$ from the curvature of the loop. He estimated the mass of the molecular cloud in the loop to be $(1.0 \pm 0.5) \times 10^{-5} M_{\odot}$. Remarkably, the center of the loop is situated in the middle between our groups B and C, and the loop itself marks the northern border of group C at this Galactic longitude. From his H1-21cm observations he found no evidence for this loop of being part of an expanding shell.

Contrary to de Geus (1992), Ortega et al. (2009), who also made an analysis of the motion of the H1 shell in Crux, found that the shell had been expanding. Between 13 and 9 Myr before present the shell increased its radius from 15 to almost 30 pc, but then met together with the UCL shell. In this case this collision could have triggered the star formation of CGYS which had its maximum about 9 Myr ago.

6. SUMMARY AND DISCUSSION

The data from the second *Gaia* data release are an invaluable tool to study the kinematics of stellar ensembles in the Milky Way. Moreover, due to its excellent photometric data, *Gaia* enables accurate determinations of stellar masses and ages from color-absolute magnitude diagram. However, it becomes apparent that that the wealth of new observations of low-mass stars in the *Gaia*

Table 4. Binary members.

Gaia ID 1	Group 1	Mass 1 (M_{\odot})	Gaia ID 2	Group 2	Mass 2 (M_{\odot})	Separation (arcsec)	Contaminants
6075310478057303936	C	0.75	6075310478050174592	C	0.24	3.232	0
6065138792911302784	Z	1.62	6065138792911300096	Z	0.13	19.413	0
5861825550891696000	A	0.20	5861825349107118976	Z	0.19	31.073	0
6065047911406764288	Z	1.37	6065047636528853888	Z	0.26	51.768	0
5894194318558985984	Z	1.17	5894194348576228992	Z	0.66	59.699	0.2
6087959014999185152	Z	0.92	6087958675701081600	Z	0.10	113.306	0.7
6090729754245639552	Z	0.39	6090730132201936256	Z	0.18	149.843	1.2
5854812388999707008	Z	1.60	5854813312408616320	A0	0.30	166.388	3.4

passbands requires new efforts to construct adequate theoretical isochrones. We studied in this paper the large complex in Lower Centaurus Crux where a few million years ago star formation has taken place. We found some 2800 stars in a cone around $(\alpha, \delta) = (186.5^\circ, -60.5^\circ)$ with a radius of 20 degrees, which we could rate as younger than 40 Myr based on the location in the $(M_G, G-G_{RP})$ CMD. Among these, 1844 stars share tangential motion compatible with a common 3-D space motion. Their distances from the Sun range from 102 to 135 pc. The total mass of the stellar and sub-stellar objects is about $700 M_{\odot}$. On top of this common motion the whole group is expanding, and expansion started about 9 Myr ago. This expansion could not be detected by Wright & Mamajek (2018) on the basis of their analysis using TGAS stars, because, most probably the accuracy of the TGAS proper motions was not sufficient. Also 9 Myr ago the peak in the star formation rate occurred with $8 \times 10^{-5} M_{\odot} yr^{-1}$.

So, the event that was responsible for the beginning of expansion could also have triggered a higher star formation rate. Or, did a collision between UCL and LCC molecular shells occur 9 Myr ago, as Ortega et al. (2009) claim, and did such a collision trigger star formation. In any case, we find that the LCC star forming region is much younger than the 18 Myr found by Mamajek et al. (2002). This may have the following reason. Their age determination was based upon main-sequence turnoff ages for Hipparcos B-type members. The vast majority of stars in our sample have masses less than $0.3 M_{\odot}$, and the ages of these pre-main-sequence stars and brown dwarfs are determined by comparing the 3 Gaia DR2 photometric bands (absolute magnitudes) with the theoretical isochrones of CIFIST, and we rely on these age marks. As the ages from Mamajek et al. (2002) are based upon high-mass stars, there may be some inconsistency on the models underlying both methods. Although the Padova isochrones are less well adapted to the observed stellar loci of low-mass stars and brown dwarfs in the $(M_G, G-G_{RP})$ CMD, we used them to determine masses and ages of stars with masses higher than $0.7 M_{\odot}$.

Given the youth of the group, the present-day mass function should not differ too much from the initial mass function of the complex. We find that a log-normal mass function with mean mass $m_c = 0.22 M_{\odot}$ and a standard deviation $\sigma = 0.64$ fits the observations quite well between 0.05 and $1.0 M_{\odot}$. We observe, however, a steeper decline in the brown dwarf regime at masses lower than 0.05, which cannot be attributed to incompleteness of our sample. In total, CGYS contains 214 brown dwarfs. There is also an excess at about $1.4 M_{\odot}$ which may have been caused by an imperfect separation between young and old stars near this mass. Our log-normal mass function differs from the canonical Chabrier mass function (Chabrier 2003) essentially by its broader standard deviation (0.64 vs. 0.55). A Chabrier type mass function was also found by Lodieu (2013) when he studied the star formation in the Upper Scorpius part of ScoCen. While the slope of the Kroupa mass function (Kroupa 2002) describes the high-mass end quite well, it fails at low-mass stars and brown dwarfs. First, the

observed maximum of our MF is at higher masses (0.2 observed vs. $0.1 M_{\odot}$ in Kroupa), and our slope in the brown dwarf regime is much steeper. The latter is also valid for a comparison of our mass function in LCC with the mass functions in the σ Orionis cluster (Béjar et al. 2011; Peña Ramírez et al. 2012), and the very young embedded open cluster RCW 38 (Mužić et al. 2017).

With members' ages ranging from 5 to 20 Myr, we detected no less than 171 circumstellar disks showing a wide variety of evolution, from full disks to debris disks. Among these, 34 are associated with brown dwarfs. The BD disks are in its majority full/evolved, and 14% of the brown dwarfs in our sample carry these.

Summing it all up, LCC is a rich star forming region very close to the Sun, and this makes it an ideal laboratory for studying very young stars and very young brown dwarfs and their circumstellar disks. The total stellar mass of our sample in LCC is about $700 M_{\odot}$, and 80% of its stars are located d between 102 and 135 pc from the Sun with a median distance of 114.5 pc. According to the ages of our objects determined from the CIFIST isochrones star formation started about 20 Myr before present and reached its maximum 9 Myr ago. This is equal to the expansion age of our CGYS. Hence the event that was responsible for this expansion, may also have been an additional trigger for star formation.

We are grateful to Ulrich Bastian from ZAH for very helpful discussions on the astrometric quality of *Gaia* DR2 and on the procedures needed to obtain an astrometrically clean sample of stars.

This study was supported by Sonderforschungsbereich SFB 881 “The Milky Way System” (subprojects B5 and B7) of the German Research Foundation (DFG). This research has made use of the SIMBAD database and of the VizieR catalogue access tool, operated at CDS, Strasbourg, France.

This work has made use of data from the European Space Agency (ESA) mission *Gaia* (<https://www.cosmos.esa.int/gaia>), processed by the *Gaia* Data Processing and Analysis Consortium (DPAC, <https://www.cosmos.esa.int/web/gaia/dpac/consortium>). Funding for the DPAC has been provided by national institutions, in particular the institutions participating in the *Gaia* Multilateral Agreement.

This publication makes use of VOSA, developed under the Spanish Virtual Observatory project supported from the Spanish MICINN through grant AyA2011-24052.

This publication makes use of data products from the Wide-field Infrared Survey Explorer, which is a joint project of the University of California, Los Angeles, and the Jet Propulsion Laboratory/California Institute of Technology, funded by the National Aeronautics and Space Administration.

Facilities: Gaia, CDS, WISE

Software: Astropy (Astropy Collaboration et al. 2013)

REFERENCES

- Andrae, R., Fouesneau, M., Creevey, O., et al. 2018, ArXiv e-prints, arXiv:1804.09374
- Astropy Collaboration, Robitaille, T. P., Tollerud, E. J., et al. 2013, A&A, 558, A33
- Baraffe, I., Chabrier, G., Allard, F., & Hauschildt, P. H. 1998, A&A, 337, 403
- Baraffe, I., Chabrier, G., Barman, T. S., Allard, F., & Hauschildt, P. H. 2003, A&A, 402, 701
- Baraffe, I., Homeier, D., Allard, F., & Chabrier, G. 2015, A&A, 577, A42
- Bayo, A., Rodrigo, C., Barrado Y Navascués, D., et al. 2008, A&A, 492, 277
- Béjar, V. J. S., Zapatero Osorio, M. R., Rebolo, R., et al. 2011, ApJ, 743, 64
- Bertelli, G., Bressan, A., Chiosi, C., Fagotto, F., & Nasi, E. 1994, A&AS, 106, 275
- Blaauw, A. 1964, ARA&A, 2, 213
- Carpenter, J. M., Wolf, S., Schreyer, K., Launhardt, R., & Henning, T. 2005, AJ, 129, 1049
- Chabrier, G. 2003, PASP, 115, 763
- Chabrier, G., Baraffe, I., Allard, F., & Hauschildt, P. 2000, ApJ, 542, 464
- Chambers, K. C., Magnier, E. A., Metcalfe, N., et al. 2016, ArXiv e-prints, arXiv:1612.05560
- Chen, C. H., Jura, M., Gordon, K. D., & Blaylock, M. 2005, ApJ, 623, 493
- Chen, C. H., Mamajek, E. E., Bitner, M. A., et al. 2011, ApJ, 738, 122
- Chen, C. H., Pecaut, M., Mamajek, E. E., Su, K. Y. L., & Bitner, M. 2012, ApJ, 756, 133
- Chereul, E., Creze, M., & Bienayme, O. 1997, in ESA Special Publication, Vol. 402, Hipparcos - Venice '97, ed. R. M. Bonnet, E. Høg, P. L. Bernacca, L. Emiliani, A. Blaauw, C. Turon, J. Kovalevsky, L. Lindegren, H. Hassan, M. Bouffard, B. Strim, D. Heger, M. A. C. Perryman, & L. Woltjer, 545–548
- Clarke, A. J., Oudmaijer, R. D., & Lumsden, S. L. 2005, MNRAS, 363, 1111
- Cotten, T. H., & Song, I. 2016, ApJS, 225, 15
- Cruz-Saenz de Miera, F., Chavez, M., Bertone, E., & Vega, O. 2014, MNRAS, 437, 391
- de Geus, E. J. 1992, A&A, 262, 258
- de Geus, E. J., de Zeeuw, P. T., & Lub, J. 1989, A&A, 216, 44
- de Zeeuw, P. T., Hoogerwerf, R., de Bruijne, J. H. J., Brown, A. G. A., & Blaauw, A. 1999, AJ, 117, 354
- de Zeeuw, T., & Brand, J. 1985, in Astrophysics and Space Science Library, Vol. 120, Birth and Evolution of Massive Stars and Stellar Groups, ed. W. Boland & H. van Woerden, 95–101
- Duchêne, G., & Kraus, A. 2013, ARA&A, 51, 269
- Españolat, C., Ingleby, L., Hernández, J., et al. 2012, ApJ, 747, 103
- Evans, D. W., Riello, M., De Angeli, F., et al. 2018, ArXiv e-prints, arXiv:1804.09368
- Feigelson, E. D., Townsley, L. K., Broos, P. S., et al. 2013, ApJS, 209, 26
- Fujiwara, H., Yamashita, T., Ishihara, D., et al. 2009, ApJL, 695, L88
- Gaia Collaboration, Brown, A. G. A., Vallenari, A., et al. 2018, ArXiv e-prints, arXiv:1804.09365
- Gregorio-Hetem, J., Lepine, J. R. D., Quast, G. R., Torres, C. A. O., & de La Reza, R. 1992, AJ, 103, 549
- Hoogerwerf, R. 2000, MNRAS, 313, 43
- Jordi, C., Gebran, M., Carrasco, J. M., et al. 2010, A&A, 523, A48
- Koenig, X. P., & Leisawitz, D. T. 2014, ApJ, 791, 131
- Kroupa, P. 2002, Science, 295, 82
- Lieman-Sifry, J., Hughes, A. M., Carpenter, J. M., et al. 2016, ApJ, 828, 25
- Lindegren, L., Hernandez, J., Bombrun, A., et al. 2018, ArXiv e-prints, arXiv:1804.09366
- Lodieu, N. 2013, MNRAS, 431, 3222
- Luhman, K. L., & Mamajek, E. E. 2012, ApJ, 758, 31
- Magnier, E. A., Chambers, K. C., Flewelling, H. A., et al. 2016, ArXiv e-prints, arXiv:1612.05240
- Mamajek, E. E., Meyer, M. R., & Liebert, J. 2002, AJ, 124, 1670
- Mannings, V., & Barlow, M. J. 1998, ApJ, 497, 330
- Marigo, P., Girardi, L., Bressan, A., et al. 2017, ApJ, 835, 77
- Marton, G., Tóth, L. V., Paladini, R., et al. 2016, MNRAS, 458, 3479
- Melis, C., Zuckerman, B., Rhee, J. H., et al. 2012, Nature, 487, 74
- . 2013, ApJ, 778, 12
- Minniti, D., Lucas, P., & VVV Team. 2017, VizieR Online Data Catalog, 2348
- Moór, A., Curé, M., Kóspál, Á., et al. 2017, ApJ, 849, 123
- Muzić, K., Schödel, R., Scholz, A., et al. 2017, MNRAS, 471, 3699
- Oh, S., Price-Whelan, A. M., Hogg, D. W., Morton, T. D., & Spergel, D. N. 2017, AJ, 153, 257
- Ortega, V. G., Jilinski, E., de la Reza, R., & Bazzanella, B. 2009, AJ, 137, 3922

- Oudmaijer, R. D., van der Veen, W. E. C. J., Waters, L. B. F. M., et al. 1992, *A&AS*, 96, 625
- Peña Ramírez, K., Béjar, V. J. S., Zapatero Osorio, M. R., Petr-Gotzens, M. G., & Martín, E. L. 2012, *ApJ*, 754, 30
- Pecaut, M. J., & Mamajek, E. E. 2016, *MNRAS*, 461, 794
- Preibisch, T., & Mamajek, E. 2008, *The Nearest OB Association: Scorpius-Centaurus (Sco OB2)*, ed. B. Reipurth, 235
- Preibisch, T., & Zinnecker, H. 1999, *AJ*, 117, 2381
- Rizzuto, A. C., Ireland, M. J., & Zucker, D. B. 2012, *MNRAS*, 421, L97
- Röser, S., Schilbach, E., & Goldman, B. 2016, *A&A*, 595, A22
- Röser, S., Schilbach, E., Goldman, B., et al. 2018, *A&A*, 614, A81
- Röser, S., Schilbach, E., Piskunov, A. E., Kharchenko, N. V., & Scholz, R.-D. 2011, *A&A*, 531, A92
- Salpeter, E. E. 1955, *ApJ*, 121, 161
- Sartori, M. J., Lépine, J. R. D., & Dias, W. S. 2003, *A&A*, 404, 913
- Scalo, J. M. 1986, *FCPh*, 11, 1
- Schneider, A., Song, I., Melis, C., Zuckerman, B., & Bessell, M. 2012, *ApJ*, 757, 163
- Skrutskie, M. F., Cutri, R. M., Stiening, R., et al. 2006, *AJ*, 131, 1163
- Wright, E. L., Eisenhardt, P. R. M., Mainzer, A. K., et al. 2010, *AJ*, 140, 1868
- Wright, N. J., & Mamajek, E. E. 2018, *MNRAS*, 476, 381